









Three-dimensional in situ imaging of single-grain growth in polycrystalline $\text{In}_2\text{O}_3:\text{Zr}$ films

Dmitry Dzhigaev ^{1✉}, Yury Smirnov², Pierre-Alexis Repecaud², Lucas Atila Bernardes Marçal ^{1,3}, Giovanni Fevola ⁴, Dina Sheyfer ⁵, Quentin Jeangros ⁶, Wonsuk Cha ⁵, Ross Harder⁵, Anders Mikkelsen¹, Jesper Wallentin ¹, Monica Morales-Masis² & Michael Elias Stuckelberger ⁴

Strain and interactions at grain boundaries during solid-phase crystallization are known to play a significant role in the functional properties of polycrystalline materials. However, elucidating three-dimensional nanoscale grain morphology, kinetics, and strain under realistic conditions is challenging. Here, we image a single-grain growth during the amorphous-to-polycrystalline transition in technologically relevant transparent conductive oxide film of $\text{In}_2\text{O}_3:\text{Zr}$ with in situ Bragg coherent X-ray diffraction imaging and transmission electron microscopy. We find that the Johnson-Mehl-Avrami-Kolmogorov theory, which describes the average kinetics of polycrystalline films growth, can be applied to the single grains as well. The quantitative analysis stems directly from imaging results. We elucidate the interface-controlled nature of the single-grain growth in thin films and reveal the surface strains which may be a driving force for anisotropic crystallization rates. Our results bring in situ imaging with coherent X-rays towards understanding and controlling the crystallization processes of transparent conductive oxides and other polycrystalline materials at the nanoscale.

¹Division of Synchrotron Radiation Research and NanoLund, Department of Physics, Lund University, P.O. Box 118, SE-22100 Lund, Sweden. ²MESA+ Institute for Nanotechnology, University of Twente, Enschede 7500 AE, The Netherlands. ³MAX IV Laboratory, Lund University, P.O. Box 118, SE-22100 Lund, Sweden. ⁴Center for X-ray and Nano Science CXNS, Deutsches Elektronen-Synchrotron DESY, Notkestr. 85, 22607 Hamburg, Germany. ⁵X-ray Science Division, Argonne National Laboratory, 9700 S Cass Ave, 60439 Lemont, IL, USA. ⁶Photovoltaics and Thin Film Electronics Laboratory, Institute of Electrical and Microengineering, École Polytechnique Fédérale de Lausanne, Rue de la Maladière 71b, 2002 Neuchâtel, Switzerland. ✉email: dmitry.dzhigaev@sljus.lu.se

Polycrystalline materials are ubiquitous in materials science and engineering applications due to a wide variety of their functional properties. This includes metals, ceramics, oxides, and semiconductors. In polycrystalline bulk materials and thin films, grain structures and interfaces directly impact mechanical, optical, thermal, magnetic, electrical, and chemical properties due to the existence of local heterogeneity in structure, composition, chemistry, and electronic structure down to the atomic scale^{1,2}. These properties can be tuned by engineering the grain structures via mechanical, thermal, chemical, and other treatments. In this work, we consider an example of transparent conductive oxides (TCOs), widely accepted as transparent electrodes in a variety of high-performance devices, such as silicon heterojunction, copper indium gallium selenide, perovskite, and silicon-based tandem solar cells. In particular, In_2O_3 -based TCOs doped with metals such as W, Ce, and Zr^{3–6}, have recently gained significant research attention due to their wide bandgap E_g and high electron mobilities μ_e . It has been shown that these TCOs are mainly amorphous when deposited at room temperature and that their transport properties improve after solid-phase crystallization by annealing at elevated temperatures^{5,7}. Studies of solid-phase crystallization phenomena in amorphous thin films are important for gaining new insights about the temporal structure-functionality relationship relevant to device optimization. Moreover, the strain fields developing both on the level of amorphous matrix and crystalline grains may drive the kinetics of crystallization. The general theory of the kinetics of phase change developed by ref. ⁸ describes average characteristics of solid-phase crystallization. However, the details of growth and strain development on the scale of a single grain are lacking, limiting our understanding of the phenomenon. Three-dimensional (3D) nanoscale imaging of such processes in situ would improve our understanding of how grains grow, interact with each other and the substrates, and influence material properties.

The amorphous-to-polycrystalline transition in In_2O_3 -based TCO films has been locally observed by top-view scanning electron microscopy with electron backscatter diffraction (EBSD)^{3,9}, as well as by transmission electron microscopy (TEM)^{7,10}. These measurements were typically performed under ex situ conditions without direct influence of reactive atmospheres and provide only 2D overview of the films, which may limit our understanding of the process. The crystallization dynamics of the whole thin film volume has been previously studied by in situ X-ray diffraction (XRD) during the annealing experiments^{3,11,12}. While electron microscopy provides close to atomic-scale resolution, the XRD technique allows following only the average crystal structure over large fields of view. Single-grain imaging with access to strain fields was realized by dark-field X-ray microscopy¹³. However, the spatial resolution has a lower limit of around 100 nm, the imaging setup requires high-quality lenses after the sample, and the strain sensitivity is limited.

Lensless Bragg coherent X-ray diffraction imaging (BCDI) addresses above-mentioned limitations by providing high-resolution 3D structure and strain in single nanoparticles under realistic conditions¹⁴. In situ 3D imaging of annealing processes, defects formation, and phase transformations in grains and nanoparticles was demonstrated in a number of recent works^{15–17}. The 3D diffraction patterns arising by coherent X-ray scattering from an isolated crystalline grain are highly sensitive to the shape and strain (down to 10^{-4})^{18,19}. Therefore, BCDI is a highly suitable technique to study single-grain growth in polycrystalline materials.

Here, we apply in situ 3D imaging of single-grain growth during the Zr-doped In_2O_3 (IZrO) film crystallization combined with in situ TEM imaging²⁰ (see Fig. 1a–e). We successfully performed 3D reconstructions of the single-grain morphology and strain evolution starting from a sub-80 nm seed particle up to its 400 nm fully crystallized state. We retrieved information about the initial stages of grain crystallization by direct analysis of the

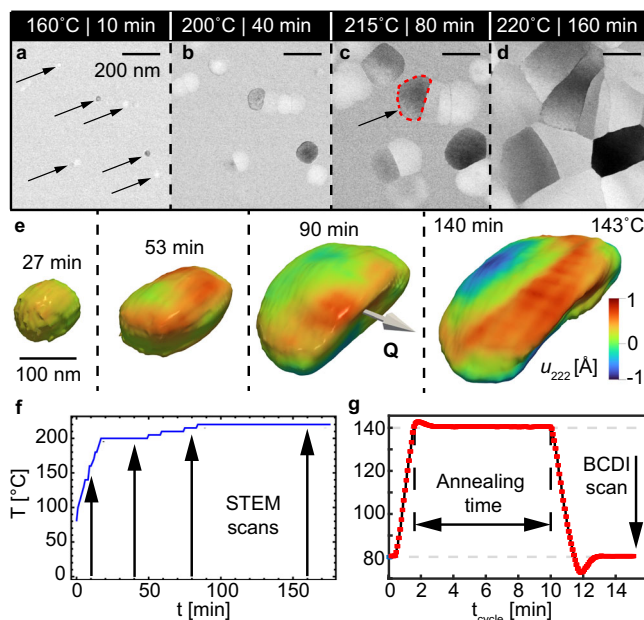


Fig. 1 In situ scanning transmission electron microscopy (STEM) and BCDI of single IZrO grain growth. **a–d** STEM bright-field micrographs capturing the IZrO film crystallization process while heating in the microscope. Arrows in **a** indicate a selection of initial crystallites, while the grain highlighted by the red dashed contour in **c** exhibits a similar morphology to that analyzed by BCDI (see the full movie of the crystallization sequence in Supplementary Movie 1). **e** Three-dimensional BCDI reconstruction of a single-grain growth during annealing of IZrO film. Color encodes displacement field $u_{222}(\mathbf{r})$. The direction of scattering vector \mathbf{Q} is shown by the white arrow in the third panel. Temperature profiles of the STEM measurement (**f**) and typical annealing cycle for the BCDI experiment (**g**).

reciprocal space intensity distribution in the vicinity of the (222) Bragg reflection. 3D evolution of the grain shape and strain distribution was obtained by phase retrieval algorithms²¹. We applied high-resolution TEM imaging to access a 2D overview of the same process in vacuum over many grains and obtained higher temporal and 2D spatial resolution. This correlative approach uniquely allows getting a more complete picture of the crystallization process. We evaluate the growth kinetics directly from imaging results employing the macroscopic Johnson-Mehl-Avrami-Kolmogorov (JMAK) theory on a single-grain level. This approach is a major step from the indirect analysis of XRD patterns reported previously^{10,22}. Our quantitative analysis of the morphology kinetics and strain development lays the experimental foundation for more detailed theories of solid-phase crystallization phenomena.

Results

Sample. Amorphous IZrO films were prepared by pulsed laser deposition (PLD) at room temperature (see “Methods” for details). The films studied by BCDI are 78 nm thick and the films analyzed by TEM are 50 nm thick. The films present good optoelectronic properties (bandgap: $E_g > 3.5$ eV; electron mobility $\mu_e > 20 \text{ cm}^2 \text{ V}^{-1} \text{ s}^{-1}$) and free carrier density of $4 \times 10^{20} \text{ cm}^{-3}$). Annealing at temperatures above 150 °C in air results in solid-phase crystallization of the films, leading to polycrystalline films with large grains, further improving the optoelectronic properties of the films: widening of the bandgap ($E_g > 3.7$ eV) and the increase of electron mobility ($\mu_e > 70 \text{ cm}^2 \text{ V}^{-1} \text{ s}^{-1}$)^{5,7,9}.

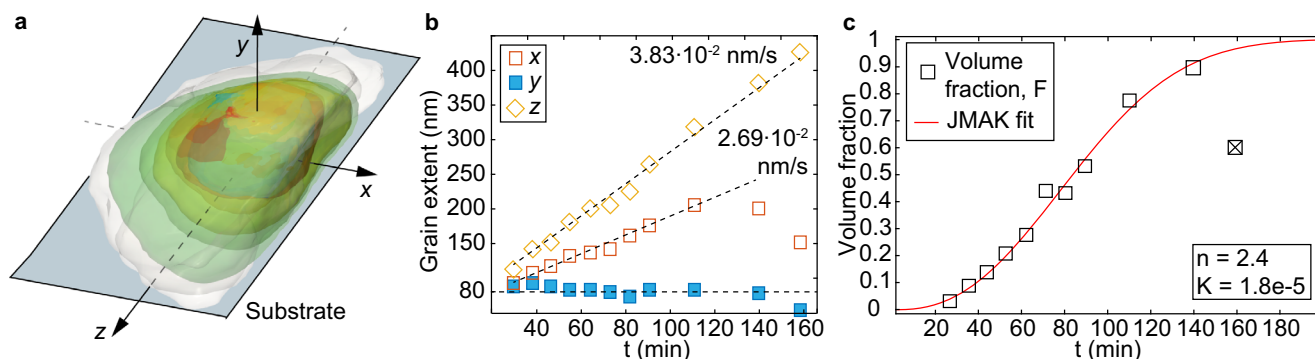


Fig. 2 Morphology and growth kinetics of a single IZrO grain. **a** Isosurfaces of amplitude $\rho(\mathbf{r})$ represent the time steps and corresponding BCDI reconstruction. All reconstructions are aligned with respect to their center of masses. The sample reference frame (x, y, z) is aligned with the substrate and principal growth directions of the grain. **b** Time dependence of the grain dimensions in the sample reference frame. Rates correspond to linear fits shown by dashed lines. **c** The volume fraction F of the IZrO grain as a function of annealing time obtained from BCDI reconstructions (black squares). The solid red line is the nonlinear fitting curve to the JMAK equation obtained by the trust-region algorithm (R^2 : 0.9884).

In situ 2D imaging of IZrO solid-phase crystallization via TEM. We first investigated the microstructure and crystallization kinetics of IZrO thin films by in situ heating during scanning TEM (see Supplementary Note 1 and Supplementary Fig. 1 for details). The IZrO films feature small crystallites dispersed in an amorphous matrix (see arrows in Fig. 1a). The crystallites then grow upon annealing inside the microscope (see Fig. 1b, c) according to the temperature profile shown in Fig. 1f. The TEM micrographs demonstrate a complicated picture of the single-grain interaction with neighbors during growth. The final image shows a dense state of the resulting polycrystalline IZrO film (see Fig. 1d). Supplementary Fig. 2b shows a zoom-out view of the crystallized film, which demonstrates that the region analyzed under the electron beam crystallized in the same way as the regions around it (non-exposed to the electron beam). That confirms that the electron beam does not influence the crystallization process. The film crystallizes according to the bixbyite In_2O_3 crystal structure, as highlighted by the atomic resolution image and the corresponding fast Fourier transform (see Supplementary Fig. 2c, d). Extending this first steady-state microstructural picture, we utilized in situ BCDI during annealing to investigate the crystallization process in 3D and assess strain fields. Note that the in situ TEM experiment was performed in a high vacuum (10^{-7} mbar), which may lead to differences in the crystallization kinetics compared to the air-annealed BCDI experiment shown below⁷.

In situ 3D imaging of IZrO solid-phase crystallization via BCDI. We applied the BCDI technique to image the evolution of a single-grain during the crystallization process. This yields the 3D structure and strain fields, complementary to electron microscopy that provides high spatial resolution in 2D. Our experiment was conducted under isothermal annealing conditions. First, the film was heated up to 81 °C from room temperature. The annealing cycle consisted of (1) a temperature ramp from 81 to 143 °C at 50 °C min^{-1} rate, (2) the actual annealing step at 143 °C, (3) the cooling down to 81 °C, initiated 10 min after starting the cycle, and (4) keeping the sample at 81 °C for the BCDI measurement. An example of the temperature profile is shown in Fig. 1g. A moderate annealing temperature of 143 °C was chosen to provide precise control over the rate of crystallization. The number of BCDI measurements was only limited by the available beamtime. The total annealing time was about 160 min, which corresponds to 80–90% of crystallization at 143 °C¹⁰. After each annealing sequence, we recorded three consecutive BCDI scans at 81 °C by performing slight sample tilts

in the vicinity of (222) Bragg condition and recording far-field diffraction patterns on the 2D detector (see Supplementary Fig. 3).

In total, 13 BCDI datasets were measured for the case of time-dependent annealing of a single IZrO grain. The first two datasets contain no coherent fringes due to a small grain size at the initial steps of crystallization. In these cases the upper limit on the grain size was estimated by employing the Scherrer equation²³ (see Supplementary Note 4 for details). The seed particle size is estimated to be 55×75 nm (x, y) after 8 min of annealing. The second dimension matches well with the thickness of the deposited film. The growth of the grain continued further in the xz -plane and is analyzed in the following section starting from 26 min of annealing.

The 3D complex-valued density of the grain $\rho(\mathbf{r})$ was reconstructed in direct space by inverting 3D diffraction data using iterative phase retrieval algorithms^{19,21}, as in the selected reconstructions shown in Fig. 1e. The modulus of this function defines the shape of the grain and is proportional to the electron density of selected crystal planes. The phase of $\rho(\mathbf{r})$ is linearly proportional to the displacement field $u(\mathbf{r})$ of atoms from their equilibrium positions as $\varphi(\mathbf{r}) = -\mathbf{Q} \cdot \mathbf{u}(\mathbf{r})$, where \mathbf{Q} is the scattering vector²⁴.

The isosurfaces of reconstruction at 25% of the maximum amplitude value allow for surface morphology evaluation (see Fig. 2a). We observe that every reconstruction ρ_i is well contained by the next one in time ρ_{i+1} . We were able to track the growth of a single particle thanks to the unique ability of BCDI to keep track of a particular grain in a polycrystalline material (see time-interpolated morphology change of the grain in Supplementary Movie 2). The BCDI scans were performed at the same temperature of 81 °C, therefore the vertical movement of the grain was negligible. The lateral movement of the grain is unlikely since it was surrounded by an amorphous matrix and other grains. Additionally, the beam footprint on the film was much larger than the grain size along incoming direction and the probability of hitting the Bragg reflection from another grain at the same position in reciprocal space was proved to be very low during the experiment. A clear vertical facet perpendicular to the substrate plane was observed in the reconstructed crystal. We attribute this feature to a grain boundary, similar to those revealed by TEM measurements in Fig. 1a. The \mathbf{Q} -vector is oriented at 19° with respect to the normal of the facet, suggesting that the boundary is (211)-oriented.

The growth rates along the facets of the grain were evaluated by extracting corresponding profiles of the amplitudes $|\rho_i|$ and

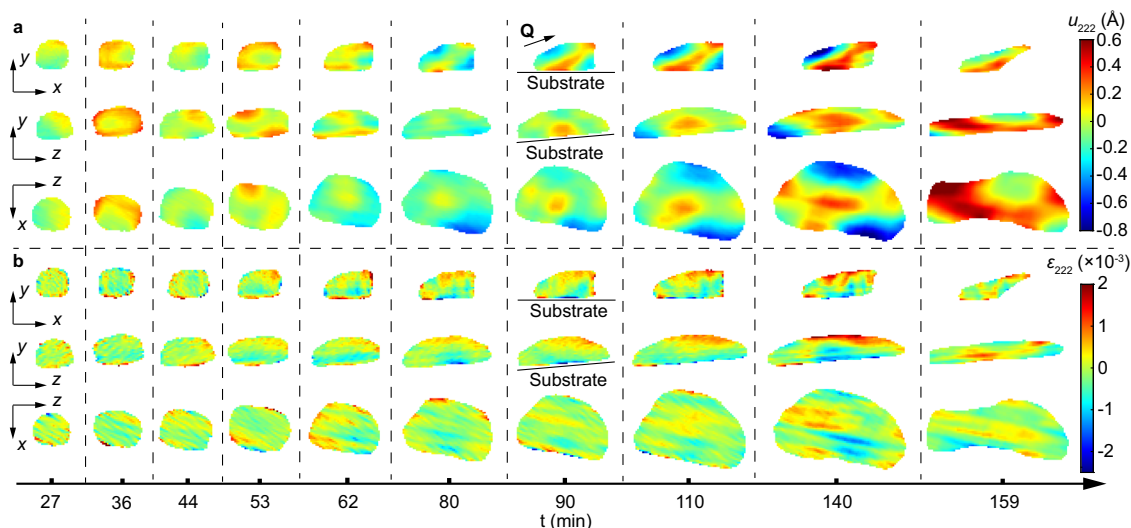


Fig. 3 Strain evolution in the IZrO grain. Orthogonal cuts through the 3D displacement (a) and strain fields (b) obtained with BCDI reconstruction of the IZrO grain as a function of annealing time. The scattering vector \mathbf{Q} is shown in a at 90 min. The lengths of coordinate axes correspond to the 100 nm scale.

calculating the width at 25% threshold (see Fig. 2b). The thickness of the grain reaches the average value of 80.7 ± 5 nm along the y -axis, which is well within the experimental error of the thickness measurement that yielded 78 nm for the as-deposited amorphous film. No additional growth was observed along y after 27 min. Crystallization rates along orthogonal x and z directions are linear and have corresponding values of $2.69 \cdot 10^{-2} \text{ nm s}^{-1}$ and $3.83 \cdot 10^{-2} \text{ nm s}^{-1}$. The last two points in the case of x -direction deviate from linear dependence due to the interaction with adjacent grains.

The volume V of the particle was evaluated by calculating the number of voxels fitting into a 3D hull at 25% of the amplitude. The corresponding normalized volume change $F = V / \max(V)$ with time is shown in Fig. 2c. The grain volume increases almost linearly with time, except for the last point where a part of the crystal was damaged/tilted and did not contribute to the Bragg peak intensity anymore.

Kinetics of grain growth. In the case of bcc In_2O_3 free micro-particles, the growth directions are determined by energies of the low index facets $\gamma_{111} < \gamma_{001} < \gamma_{110}$ ²⁵. However, this relation is violated in the complex interplay between the substrate, neighboring grains, and amorphous matrix.

Under isothermal conditions, the thermodynamics determining the nucleation and growth is expected to be constant, and the fractional amount of crystallization as a function of time $F(t)$ can be described by the JMAK equation⁸:

$$F(t) = 1 - \exp(-Kt^n), \quad (1)$$

where K is a temperature-dependent constant related to the nucleation and growth rates of the crystalline phase. The second constant, n , is the kinetic or Avrami exponent, which indicates the mechanisms of the amorphous-to-crystalline transition, its dimensionality, and typically has values between 1 and 4²⁶. We stress that this model describes an averaged behavior of polycrystalline materials and has not been tested on a single-grain level. Importantly, in the case of BCDI reconstructions we have direct access to the crystalline volume of the crystal-amorphous system confined by the interaction volume between the sample and the X-ray beam. Therefore, the fraction can be obtained as a normalized volume of the grain F . The JMAK curve was fitted to our experimental data with the maximum F value reaching 90% of crystallization (see Fig. 2c). This assumption is

supported by the fact that the last data point was measured when the grain impinged adjacent crystallites and consequently deformed. The resulting fitting parameter values are $K = 1.6 \cdot 10^{-5}$ and $n = 2.4$ (see “Methods” for details). These values are in good agreement with the reports for indium oxide films studied by XRD and accessing averaged structure and dynamics^{9,10}. With this quantitative analysis we can conclude that a single-grain growth as measured by BCDI follows the growth kinetics which can be described by JMAK theory applied directly to imaging results. Moreover, in situ BCDI directly accesses strain fields and grain deformation as a function of annealing time, which becomes more important in the light of TCO thickness reduction in solar cells or ever-shrinking scales of nanodevices employing TCOs^{27,28}.

Further, we analyzed the spatial distribution of local crystal deformation that may affect the growth of a single-grain. The 3D displacement field was extracted from the phase of the object as $u_{222}(\mathbf{r}) = -\varphi(\mathbf{r})/|\mathbf{Q}|$. The corresponding strain fields were calculated as:

$$\varepsilon_{222}(\mathbf{r}) = \nabla \mathbf{u}(\mathbf{r}) \cdot \hat{\mathbf{n}}_{\mathbf{Q}}, \quad (2)$$

where $\hat{\mathbf{n}}_{\mathbf{Q}} = \mathbf{Q}/|\mathbf{Q}|$ is a unit vector. The orthogonal cuts through the displacement and strain fields are shown in Fig. 3. The displacement field maps demonstrate local variation patterns that are traceable throughout the crystallization snapshots. As the annealing proceeded, the absolute values of u_{222} increased and lead to plastic deformation of the grain at the last step. The orthogonal cuts through 3D strain distributions reveal compressive strain at the substrate-grain boundary. Most of the outer surface of the grain shows tensile strain, especially over the second half of the annealing process. A more detailed picture of the strain evolution was extracted in line profiles along sample axes x, y, z shown in Fig. 4. The edge enhancement of absolute strain values is visible in each set of profiles. In the case of out-of-plane direction, Fig. 4, we observed the change of the strain from tensile to compressive at the crystallite/substrate interface (shown by arrows), revealing a complex interplay between grain surface energy and interaction with neighboring particles and the amorphous matrix. Correspondingly, the interface-controlled growth may be affected by the strain building up at the boundaries.

It is important to note the influence of oxygen from the air on the kinetics of grain growth. The crystallization of IZrO was

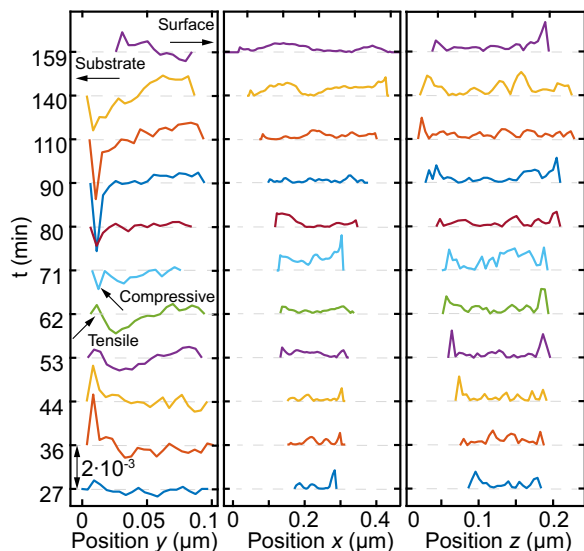


Fig. 4 Line profiles of the strain extracted from BCDI reconstructions at each time step in the annealing process. The axes correspond to those in Fig. 2a. All the graphs are on the same scale with a constant shift of $2 \cdot 10^{-3}$ for clarity.

previously assessed in various atmospheres (O_2 , N_2 , H_2), suggesting that oxygen accelerates the crystallization kinetics⁷. Based on Rutherford backscattering spectrometry data, it was suggested in ref. ²⁹, that O_2 may be able to absorb, dissociate, and diffuse into the film during annealing. This may reduce the local strains due to oxygen deficiencies and hence lower the crystallization threshold. Our results confirm previous observations in In_2O_3 -based TCOs, revealing that surface strains may be a driving force for anisotropic crystallization rates in these materials^{30,31}.

Another grain reconstruction is shown in the Supplementary Note 6 and Supplementary Fig. 7. It demonstrates that some grains have more complex structure, including defects, and growth kinetics confined by neighboring particles. The accuracy of the BCDI reconstructions is limited by spatial resolution and time sampling. Moreover, the spatial resolution is not a constant value throughout the measurement of the particle with increasing volume and highly anisotropic due to the asymmetric shape of the grain. The spatial resolution of the reconstruction varies from 50 nm to below 20 nm, as it was estimated by evaluating line spread functions at the known edges of the particle (see Supplementary Note 7 for details).

With the demonstrated approach, we foresee statistically more significant measurements will be possible at 4th generation synchrotron sources including Advanced Photon Source Upgrade Project³², PETRA IV³³, ESRF-EBS³⁴, MAX IV³⁵. With increased coherent photon flux, faster scans will become possible with improved spatial and temporal resolution. Specifically, one could access the initial stages of crystallites nucleation, when the sizes of the particles are below 50 nm. The method of in situ BCDI is relevant to other grain-growth phenomena, such as, for example, Ostwald ripening³⁶.

Conclusion

In conclusion, we performed 3D in situ imaging of single-grain growth in a functional polycrystalline TCO film. We devised an approach for analysis of kinetics of a single-grain growth directly from 3D BCDI results, extending the applicability of JMAK theory of solid-phase crystallization. With the advance of 4th generation synchrotron sources and X-ray free-electron lasers, the earlier stages of crystallization will be accessible and

spatiotemporal resolution significantly improved. Combined with advanced phasing algorithms and machine learning approaches for rapid data analysis, in situ BCDI is a powerful tool for nanoscale characterization of dynamics in polycrystalline materials.

Methods

Preparation of IZrO thin films. IZrO thin films were fabricated by wafer-based PLD at room temperature onto monocrystalline Si substrates in planar configuration coated with hydrogenated amorphous Silicon (a-Si:H) layers deposited via plasma-enhanced chemical vapor deposition (similar substrates are used for SHJ solar cell fabrication³⁷). The IZrO target (98/2 wt% In_2O_3/ZrO_2) was ablated with KrF excimer laser ($\lambda = 248$ nm) with the repetition rate of 20 Hz and the fluence of 1.9 J cm^{-2} . The total working pressure was 0.02 mbar with an oxygen total flow ratio $r(O_2) = Q(O_2)/(Q(Ar + O_2))$ of 20% as demonstrated previously⁹. The thickness of the IZrO layer was 78 nm as derived from the surface step height obtained by stylus profilometry measurements.

Scanning transmission electron microscopy. The 50 nm-thick IZrO film dedicated for TEM analysis was deposited by PLD directly on a microelectromechanical systems (MEMS) chip with heating capabilities from DENSSolutions. The IZrO-coated MEMS chip was mounted on a double-tilt holder and introduced in an image- and probe-corrected Thermo Fisher Scientific Titan Themis electron microscope. Experiments were performed in STEM mode at 200 kV with a probe current of 400 pA (see Supplementary Note 1). The electron dose was kept low and the sample was observed at a low magnification not to influence the crystallization kinetics.

Synchrotron experiment. The BCDI measurements were performed remotely with minimal intervention from the beamline staff at the 34-ID-C beamline at the Advanced Photon Source (Argonne National Laboratory, USA). Raw datasets and meta-data are available online³⁸. The amorphous IZrO film was mounted on a heater cell available at the beamline (see Supplementary Fig. 3a). The temperature values presented in this work were calibrated before the BCDI experiment (see Supplementary Table 1 in Supplementary Note 2). An X-ray beam with a photon energy of 9 keV ($\lambda = 1.38$ Å) was focused down to 800 nm \times 600 nm ($h \times v$) at full width at half maximum using Kirkpatrick-Baez mirrors³⁹. The Timepix 2D detector (Amsterdam Scientific Instruments) with a GaAs sensor and pixel size of 55 $\mu m \times$ 55 μm was positioned at the double Bragg angle $2\theta_B \approx 27^\circ$ of the (222) reflection of IZrO. The distance from the sample to the detector was adjusted during the measurements to ensure that the diffraction patterns were oversampled⁴⁰. The incoming X-ray beam had a fixed low incidence angle of 5° to maximize the footprint on the sample. The focal spot size of the X-ray beam was large enough to fully illuminate grains up to 500 nm in scale. This geometry allowed for fast scanning of films at fixed detector position and increased the probability of finding (222)-oriented seed particles. The signal from seed particles was recognized by faint Bragg peaks appearing on the 2D detector during the scan. The BCDI scans were generally performed in the angular range of 0.6° with a step size of 0.006° . After each annealing step, at least 3 rocking curves were recorded. Thermal expansion of the sample stage and drifts of the IZrO crystal were compensated by the realignment of scanning and rocking curve motors after each annealing cycle based on a confocal microscope (coarse alignment) and diffraction intensity (fine alignment). The Bragg peak was always positioned close to the center of detector module to avoid gaps in the recorded data. The resulting datasets were aligned in 3D with sub-pixel accuracy⁴¹ based on the maximum cross-correlation coefficient and summed up later to improve the signal-to-noise ratio in the data (see Supplementary Note 3 and Supplementary Fig. 4 for details).

Sample post-characterization. We performed additional electron backscattering (EBSD) measurement after the beamtime at DESY Nanolab⁴². It proved the polycrystalline nature of the IZrO film (see Supplementary Note 2 and Supplementary Fig. 2 for details). XRD was performed on the same sample at the laboratory source at Lund University and revealed bixbyite In_2O_3 crystal structure (see Supplementary Note 3 and Supplementary Fig. 5 for details).

Phase retrieval. The iterative phase retrieval was performed by employing a combination of Error-Reduction (ER), Hybrid Input-Output (HIO) algorithms. We used in total 620 iterations by repeating the combination of 20 ER and 180 HIO. The guided approach was used for five generations, with a population of ten per generation^{21,43}. The selection rule for the best candidate of the complex-valued object $\rho_i(r)$ in each generation was based on the highest value of sharpness metric $S = \sum |\rho(r)|^4$ and breeding of new estimates of the object for the new generation is calculated as $\rho_i^*(r) = \sqrt{\rho_i(r)\rho_{best}(r)}$. The final error-metric $E = \sum_Q ||\mathcal{F}(\rho(Q))|^2 - I(Q)||$ reached the lowest value of about 2% in the case of both domains. The complex-conjugate solutions to the phase retrieval problem were filtered in the direct space by the orientation of flat facet of the grain since it is expected to be facing Si substrate. The phase ramps were removed from the reconstructed objects before quantitative analysis.

Kinetics of grain growth. In general, the Avrami exponent $n = 2.4$ is not constant during the crystallization and can be expanded in the following form⁴⁴ $n = b + pm$, where b is the nucleation index, p is the growth index between 0.5 and 1, and m denotes the d -dimensional grain growth. In our case, $b = 0$ since there is only a single nucleation event, $m = 2$ since the 3D growth is limited by the thickness of the amorphous film, and $p = 1$ since the growth is mainly interface-controlled¹⁰. In polycrystalline thin films, the grain growth does not strictly follow classical JMAK theory, therefore the local values of the Avrami exponent as a function of crystalline fraction $n(F)$ were evaluated following ref. ⁴⁵ (see Supplementary Note 5 and Supplementary Fig. 6 for details). The mean value of $\langle n(F) \rangle = 2.5$ is remarkably close to the one obtained by JMAK fit of crystalline fraction, while providing values of around 4 at the beginning of the process. It is important to note that the exact values of the extracted parameters may differ due to additional crystallization happening during temperature ramp-up/-down (see Fig. 1g). The crystallization rates are expected to be much lower in these regions and annealing time may be increased by 1–2 min.

Data availability

The datasets generated during the current study are available in the Zenodo repository, <https://doi.org/10.5281/zenodo.6532951>.

Code availability

The codes developed during the current study are available from the corresponding author on reasonable request.

Received: 2 February 2022; Accepted: 23 May 2022;

Published online: 17 June 2022

References

- Ashby, M. F., Shercliff, H. & Cebon, D. *Materials: Engineering, Science, Processing and Design* (Butterworth-Heinemann, 2018).
- Ulvestad, A. et al. Multimodal X-ray imaging of grain-level properties and performance in a polycrystalline solar cell. *J. Synchrotron Radiat.* **26**, 1316–1321 (2019).
- Koida, T., Ueno, Y. & Shibata, H. In₂O₃-based transparent conducting oxide films with high electron mobility fabricated at low process temperatures. *Phys. Status Solidi (a)* **215**, 1700506 (2018).
- Morales-Masis, M. et al. Highly conductive and broadband transparent Zr-doped In₂O₃ as front electrode for solar cells. *IEEE J. Photovolt.* **8**, 1202–1207 (2018).
- Aydin, E. et al. Zr-doped indium oxide (IZRO) transparent electrodes for perovskite-based tandem solar cells. *Adv. Funct. Mater.* **29**, 1901741 (2019).
- Tutsch, L. et al. The sputter deposition of broadband transparent and highly conductive cerium and hydrogen co-doped indium oxide and its transfer to silicon heterojunction solar cells. *Prog. Photovolt. Res. Appl.* **29**, 835–845 (2021).
- Rucavado, E. et al. Zr-doped indium oxide electrodes: annealing and thickness effects on microstructure and carrier transport. *Phys. Rev. Mater.* **3**, 084608 (2019).
- Avrami, M. General theory. *J. Chem. Phys.* **7**, 103–112 (1939).
- Smirnov, Y. et al. Scalable pulsed laser deposition of transparent rear electrode for perovskite solar cells. *Adv. Mater. Technol.* **6**, 2000856 (2021).
- Jia, J. et al. Temporal evolution of microscopic structure and functionality during crystallization of amorphous indium-based oxide films. *ACS Appl. Mater. Interfaces* **13**, 31825–31834 (2021).
- Wardenga, H. F., Frischbier, M. V., Morales-Masis, M. & Klein, A. In situ hall effect monitoring of vacuum annealing of In₂O₃:H thin films. *Materials* **8**, 561–574 (2015).
- Wang, M. et al. Thermal crystallization kinetics and crystallite size distribution of amorphous ITO film deposited in the presence or absence of water vapor. *Thin Solid Films* **518**, 2992–2995 (2010).
- Simons, H. et al. Dark-field x-ray microscopy for multiscale structural characterization. *Nat. Commun.* **6**, 1–6 (2015).
- Pfeifer, M. A., Williams, G. J., Vartanyants, I. A., Harder, R. & Robinson, I. K. Three-dimensional mapping of a deformation field inside a nanocrystal. *Nature* **442**, 63–66 (2006).
- Ulvestad, A. et al. Topological defect dynamics in operando battery nanoparticles. *Science* **348**, 1344–1347 (2015).
- Yau, A., Cha, W., Kanan, M. W., Stephenson, G. B. & Ulvestad, A. Bragg coherent diffractive imaging of single-grain defect dynamics in polycrystalline films. *Science* **356**, 739–742 (2017).
- Yang, D. et al. Annealing of focused ion beam damage in gold microcrystals: an in situ Bragg coherent x-ray diffraction imaging study. *J. Synchrotron Radiat.* **28**, 550–565 (2021).
- Robinson, I. & Harder, R. Coherent x-ray diffraction imaging of strain at the nanoscale. *Nat. Mater.* **8**, 291–298 (2009).
- Clark, J. N. et al. Three-dimensional imaging of dislocation propagation during crystal growth and dissolution. *Nat. Mater.* **14**, 780–784 (2015).
- Moghadam, M. M. et al. In situ crystallization and morphological evolution in multicomponent indium oxide thin films. *Cryst. Growth Des.* **17**, 1396–1403 (2017).
- Fienup, J. R. Phase retrieval algorithms: a personal tour. *Appl. Opt.* **52**, 45–56 (2013).
- Macco, B. et al. On the solid phase crystallization of In₂O₃:H transparent conductive oxide films prepared by atomic layer deposition. *J. Appl. Phys.* **120**, 085314 (2016).
- Patterson, A. The scherrer formula for x-ray particle size determination. *Phys. Rev.* **56**, 978 (1939).
- Dzhigaev, D. et al. Bragg coherent x-ray diffractive imaging of a single indium phosphide nanowire. *J. Opt.* **18**, 064007 (2016).
- Meng, M. et al. Cubic In₂O₃ microparticles for efficient photoelectrochemical oxygen evolution. *J. Phys. Chem. Lett.* **5**, 4298–4304 (2014).
- Li, W. & Wang, T. Ab initio investigation of the elasticity and stability of aluminium. *J. Phys. Condens. Matter* **10**, 9889 (1998).
- Wallentin, J. et al. InP nanowire array solar cells achieving 13.8% efficiency by exceeding the ray optics limit. *Science* **339**, 1057–1060 (2013).
- Otnes, G. et al. Understanding InP nanowire array solar cell performance by nanoprobe-enabled single nanowire measurements. *Nano Lett.* **18**, 3038–3046 (2018).
- Nastasi, M., Mayer, J. W. & Wang, Y. *Ion Beam Analysis: Fundamentals and Applications* (CRC Press, 2014).
- Jia, J. et al. Formation of homologous In₂O₃(ZnO)_m thin films and its thermoelectric properties. *J. Vac. Sci. Technol. A Vac. Surf. Films* **34**, 041507 (2016).
- Suko, A. et al. Crystallization behavior of amorphous indium–gallium–zinc-oxide films and its effects on thin-film transistor performance. *Jpn J. Appl. Phys.* **55**, 035504 (2016).
- Fornet, T. E. *Advanced Photon Source Upgrade Project Final Design Report*. Tech. Rep. (2019).
- Schroer, C. G. et al. PETRA IV: the ultralow-emittance source project at DESY. *J. Synchrotron Radiat.* **25**, 1277–1290 (2018).
- Raimondi, P. ESRF-EBS: the extremely brilliant source project. *Synchrotron Radiat. News* **29**, 8–15 (2016).
- Tavares, P. F. et al. Commissioning and first-year operational results of the MAX IV 3 GeV ring. *J. Synchrotron Radiat.* **25**, 1291–1316 (2018).
- Ostwald, W. Studien über die bildung und umwandlung fester körper. *Zeitschrift für physikalische Chemie* **22**, 289–330 (1897).
- Bivour, M., Schröer, S., Hermle, M. & Glunz, S. W. Silicon heterojunction rear emitter solar cells: Less restrictions on the optoelectrical properties of front side tcso. *Sol. Energy Mater. Sol. Cells* **122**, 120–129 (2014).
- Dzhigaev, D. et al. Three-dimensional in-situ imaging of single-grain growth in polycrystalline In₂O₃:Zr films [Data sets]. <https://doi.org/10.5281/zenodo.6532951>. Zenodo. (2022).
- Kirkpatrick, P. & Baez, A. V. Formation of optical images by x-rays. *JOSA* **38**, 766–774 (1948).
- Sayre, D. Some implications of a theorem due to Shannon. *Acta Crystallogr.* **5**, 843–843 (1952).
- Guizar-Sicairos, M., Thurman, S. T. & Fienup, J. R. Efficient subpixel image registration algorithms. *Opt. Lett.* **33**, 156–158 (2008).
- Stierle, A., Keller, T. F., Noei, H., Vonk, V. & Roehlsberger, R. DESY nanolab. *J. Large-Scale Res. Facil.* **2**, 76 (2016).
- Ulvestad, A. et al. Identifying defects with guided algorithms in bragg coherent diffractive imaging. *Sci. Rep.* **7**, 1–9 (2017).
- Gao, Q. et al. Crystallization kinetics of the Cu₅₀Zr₅₀ metallic glass under isothermal conditions. *J. Solid State Chem.* **244**, 116–119 (2016).
- Calka, A. & Radlinski, A. The local value of the Avrami exponent: a new approach to devitrification of glassy metallic ribbons. *Mater. Sci. Eng.* **97**, 241–246 (1988).

Acknowledgements

This research was funded by the European Research Council (ERC) under the European Union's Horizon 2020 research and innovation program (Grant Agreement 801847). This project also has the funding support from the Olle Engkvist Foundation and NanoLund. This research used resources of the Advanced Photon Source, a U.S. Department of Energy (DOE) Office of Science User Facility operated for the DOE Office of Science by Argonne National Laboratory under Contract No. DE-AC02-06CH11357. Y.S., P.A.R., M.M.–M acknowledge the support from the SOLAR ERA NET, project CUSTCO, number SOL18001. Q.J. aims to acknowledge the Swiss National Science Foundation (project Nachos: 200021L 172924). V. Tileli and R. Ignatans are gratefully

acknowledged for providing access to the in situ heating TEM holder. The research leading to these results has received funding from Deutsches Elektronen-Synchrotron DESY and we would like to thank Arno Jeromin from DESY NanoLab for performing EBSD measurements.

Author contributions

D.D., M.E.S., and M.M.-M. conceived the idea of the project; P.-A.R., Y.S., and M.M.-M. prepared the samples; D.D., L.A.B.M., G.F., D.S., W.C., R.H., A.M., J.W., and M.E.S. performed the synchrotron experiment; Q.J. performed in situ electron microscopy measurements; D.D. performed data analysis and prepared the manuscript with contributions from all authors.

Funding

Open access funding provided by Lund University.

Competing interests

The authors declare no competing interests.

Additional information

Supplementary information The online version contains supplementary material available at <https://doi.org/10.1038/s43246-022-00260-4>.

Correspondence and requests for materials should be addressed to Dmitry Dzhigaev.

Peer review information *Communications Materials* thanks the anonymous reviewers for their contribution to the peer review of this work. Primary Handling Editors: Andreja Benčan Golob and Aldo Isidori. Peer reviewer reports are available.

Reprints and permission information is available at <http://www.nature.com/reprints>

Publisher's note Springer Nature remains neutral with regard to jurisdictional claims in published maps and institutional affiliations.



Open Access This article is licensed under a Creative Commons Attribution 4.0 International License, which permits use, sharing, adaptation, distribution and reproduction in any medium or format, as long as you give appropriate credit to the original author(s) and the source, provide a link to the Creative Commons license, and indicate if changes were made. The images or other third party material in this article are included in the article's Creative Commons license, unless indicated otherwise in a credit line to the material. If material is not included in the article's Creative Commons license and your intended use is not permitted by statutory regulation or exceeds the permitted use, you will need to obtain permission directly from the copyright holder. To view a copy of this license, visit <http://creativecommons.org/licenses/by/4.0/>.

© The Author(s) 2022